

Article

Self-Heating and Fatigue Assessment of Laser Powder Bed Fusion NiTi Alloy with High Cycle Fatigue Mechanisms Identification

Timothee Cullaz ^{1,2}, Luc Saint-Sulpice ² , Mohammad Elahinia ¹  and Shabnam Arbab Chirani ^{3,*} 

- ¹ Mechanical Industrial and Manufacturing Engineering Department, University of Toledo, Toledo, OH 43606, USA; timothee.cullaz@rockets.utoledo.edu (T.C.); mohammad.elahinia@utoledo.edu (M.E.)
- ² ENI Brest, UMR CNRS 6027, IRDL, 29200 Brest, France; sulpice@enib.fr
- ³ ENSTA Bretagne, UMR CNRS 6027, IRDL, 29200 Brest, France
- * Correspondence: shabnam.arbab@ensta-bretagne.fr

Abstract: Rapid methods for assessing the fatigue properties of materials have been developed, among which the self-heating method stands out as particularly promising. This approach analyzes the thermal signal of the specimen when subjected to cyclic loading. In this research, the self-heating method was utilized for the first time with laser powder bed fusion (LPBF) of NiTi alloys, examining two specific loading conditions: loading ratios of 0.1 and 10. A thorough examination of the material self-heating behavior was conducted. For comparative purposes, conventional fatigue tests were also conducted, alongside interrupted fatigue tests designed to highlight the underlying mechanisms involved in high cycle fatigue and potentially self-heating behavior. The investigation revealed several key mechanisms at play, including intra-grain misorientation, the emergence and growth of persistent slip bands, and the formation of stress-induced martensite. These findings not only deepen our understanding of the fatigue behavior of LPBF NiTi alloys but also highlight the self-heating method potential as a tool for studying material fatigue.

Keywords: 3D printing; self-heating; high cycle fatigue; shape memory alloy; fatigue mechanisms



Citation: Cullaz, T.; Saint-Sulpice, L.; Elahinia, M.; Arbab Chirani, S. Self-Heating and Fatigue Assessment of Laser Powder Bed Fusion NiTi Alloy with High Cycle Fatigue Mechanisms Identification. *Metals* **2024**, *14*, 496. <https://doi.org/10.3390/met14050496>

Academic Editor: Hany Hassanin

Received: 22 March 2024

Revised: 12 April 2024

Accepted: 16 April 2024

Published: 24 April 2024



Copyright: © 2024 by the authors. Licensee MDPI, Basel, Switzerland. This article is an open access article distributed under the terms and conditions of the Creative Commons Attribution (CC BY) license (<https://creativecommons.org/licenses/by/4.0/>).

1. Introduction

Shape memory alloys (SMAs) present potential in many applications, such as biomedical devices and aerospace, automotive, and civil engineering due to their unique superelasticity, shape memory effect, and elastocaloric properties [1–12]. These properties are due to a reversible martensitic transformation [13]. Among them, superelasticity stands out due to its exceptional mechanical behavior. The material can undergo large elastic deformations and recover its strain when the stress is released. Superelasticity is attributed to the reversible phase transformations between the austenite phase (*A*) and the martensite phase (*M*). These transformations are triggered by stress under isothermal conditions [13,14]. To observe the superelasticity, the material needs to be fully austenitic, thus, the service temperature must be higher than the martensite start temperature (M_s). Then, during the loading, the direct transformation will occur when the austenite phase transforms into a martensite phase. When the stress is released, the martensite phase transforms back into an austenite phase. This is referred to as reverse transformation.

For a few decades now, research teams have been able to fabricate NiTi via additive manufacturing (AM) processes especially via laser powder bed fusion (LPBF). The opportunities that this innovative fabrication process opens are multiple. Complex geometry like lattice structure are now possible [15]; the possibility to tune the material properties by optimizing the process parameters in order to enhance the performances has been highly investigated [16,17]. This technology allows also the fabrication of functionally graded material [18,19]. However, LPBF requires process parameters tuning to prevent the defect

population characteristic of the process. Nevertheless, defects can remain even after a process parameter optimization [16].

The fatigue behavior of SMAs, including NiTi, has gained significant attention in various applications, particularly focusing on low cycle fatigue (LCF) [20–23]. However, research specifically addressing high cycle fatigue (HCF) in additive manufactured NiTi remains limited [24,25]. These studies have highlighted that fatigue failure in additive manufactured NiTi is largely influenced by internal defects introduced during the fabrication process. The location, shape, and size of these defects can significantly impact premature failure. Although the standard determination method for HCF, as prescribed by ASTM specifications, is considered the reference [26], it is both time and specimen-consuming, requiring numerous specimens and several days for each fatigue test at the selected frequency.

Since the 2000s, several research studies have proposed an alternative approach for rapid prediction of HCF properties, leveraging the thermal signal emitted by the specimen under cyclic loading across different materials [27–30]. This method, known as the self-heating method, offers a faster evaluation of HCF properties. This recent approach is based on specific cyclic loading and the measurement of temperature elevation under this cyclic loading. It has been applied in various materials [29,31–37], including conventional shape memory alloys [38,39].

The objective of the present study is to qualify the self-heating behavior and fatigue properties of LPBF-NiTi. Furthermore, this study intends to investigate the possible relationship between the self-heating behavior and fatigue in this material. The findings of this work may be helpful toward a model that can describe the self-heating behavior and predict the fatigue properties following the method presented by Doudard et al. [27].

2. Materials and Methods

2.1. Studied Material

For the specimen fabrication, a commercial pre-alloyed NiTi powder was selected that was produced by gas atomization from Ni_{50.8}Ti (at%) annealed ingots (Confluent Medical Technology Inc., Fremont, CA, USA). The powder exhibits a particle size distribution ranging from 15 to 75 µm. For the specimens fabrication, a Phoenix PXM 3D printer (3D Systems Inc., Rock Hill, SC, USA) with a wavelength of 1070 nm and a beam size of 80 µm was used. The oxygen level was maintained at a level lower than 600 ppm during the fabrication. The process parameters were set to optimize fabrication conditions, guided by prior studies focusing on parameter optimization [40]. Specifically, the laser power (P), scanning velocity (v), hatch spacing (h), layer thickness (t), and scanning strategy were configured to 250 W, 1250 mm/s, 80 µm, 30 µm, and 90°, respectively. These parameters collectively yield a volumetric energy density described by the equation $E = \frac{P}{v \cdot h \cdot t} = 83 \text{ J/mm}^3$.

Two distinct batches of specimens were manufactured for the purpose of this study. Batch 1 consisted of a dozen cubic specimens, each measuring 4 mm × 4 mm × 4 mm. Batch 2 comprised 20 tensile specimens, fabricated under identical process parameters as the previous batch. These specimens, as illustrated in Figure 1 with the building direction, were specifically designed to explore cyclic tensile behavior. In the figure, the hatched zone denotes the support structure necessary during fabrication. Subsequent to the fabrication process, the support structures were extracted, and the specimens underwent manual polishing.

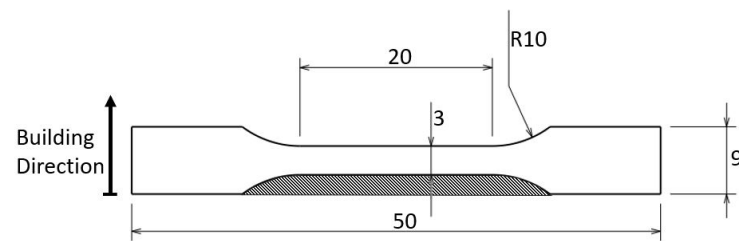


Figure 1. Printed part geometry and the building orientations of tensile flat specimen (Batch 2). Thickness is 2 mm.

2.2. Thermomechanical Properties

The phase transformation temperatures of the material were investigated using a DSC250 differential scanning calorimeter from TA Instruments (New Castle, DE, USA), as shown in Figure 2. The DSC experiments were conducted with cooling and heating rates set at 10 K/min, ranging from $-75\text{ }^{\circ}\text{C}$ to $75\text{ }^{\circ}\text{C}$. The martensite start temperature (M_s) and austenite finish temperature (A_f) of Batch 1 specimens were determined to be $6\text{ }^{\circ}\text{C}$ and $15\text{ }^{\circ}\text{C}$, respectively. For the tensile specimens, the M_s and A_f temperatures were found to be $-9\text{ }^{\circ}\text{C}$ and $13\text{ }^{\circ}\text{C}$, respectively (see Table 1). This indicates that the material exhibits superelastic behavior at room temperature in both geometries. Specifically, at room temperature ($T_{amb} = 25\text{ }^{\circ}\text{C}$), only the austenite phase is present. It is important to note that the peak width observed in the DSC measurements may vary due to inherent variability induced by the LPBF process [41].

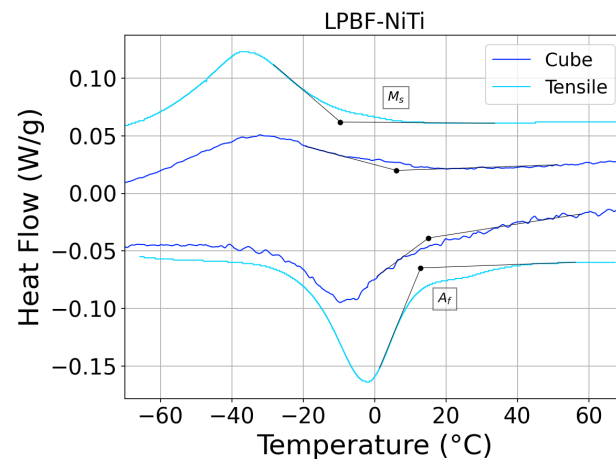


Figure 2. DSC results for cube and tensile specimens with the identification of the characteristic temperatures A_f , and M_s .

Table 1. Transformation temperatures of LPBF-NiTi.

Specimen	M_s ($^{\circ}\text{C}$)	A_f ($^{\circ}\text{C}$)
Cube	6	15
Tensile	-9	13

Tensile and compression uniaxial tests were conducted at a strain rate of $2 \times 10^{-4}\text{ s}^{-1}$ at room temperature utilizing an Instron E10000 electrodynamic testing machine. The strain for tensile tests was measured using an extensometer set on the gauge length of the specimen. Conversely, due to the smaller size of the setup, digital image correlation (DIC) with a 12 M GOM ARAMIS setup was employed to measure compression strains. As depicted in Figure 3, loading–unloading curves were observed. The material exhibits a transformation plateau with a low residual strain. Notably, material properties such as the transformation yield stress, also called the phase transformation limit (σ_0), can be

determined. Thus, σ_0 for compression samples was found to be 283 MPa, whereas for tensile samples, it was 425 MPa.

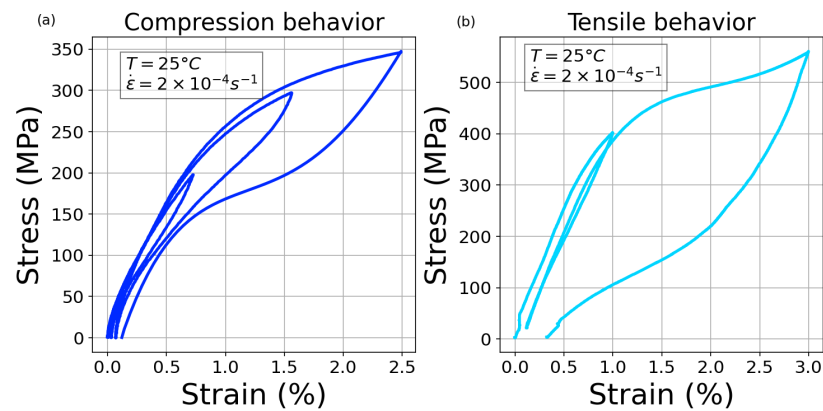


Figure 3. Stress–strain curves of the uniaxial (a) compression test and (b) tensile tests.

2.3. Cyclic Experimental Setup

The cyclic tests, including fatigue and self-heating tests, were performed on a Instron (Norwood, MA, USA) E10000 electrodynamic testing machine. The temperature was measured with a IR camera (Infratec (Dresden, Germany) ImageIR 8300HP) as a temperature average in the white rectangles in Figure 4. For the self-heating tests, the specimens were painted with a black paint to maximize the emissivity in order to measure the true thermal signal from the specimens. In addition, a thick cover was installed around the whole setup to prevent any thermal variation from the environment.

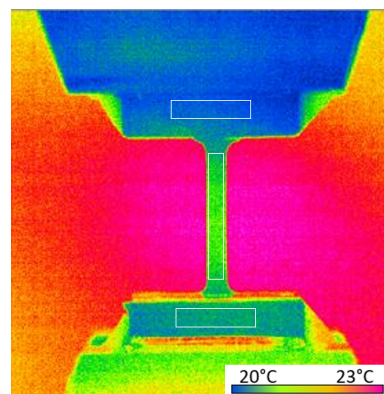


Figure 4. Infrared image captured of one specimen with three average temperatures measured in the white rectangles for specimen and grips.

The self-heating test comprises cyclic loading, known as loading blocks, with each block consisting of 3000 cycles at a frequency of $f_r = 30$ Hz and a maximal stress under load control (see Figure 5a). In compression self-heating tests, the initial maximal stress starts at $\sigma_{max} = 80$ MPa with a loading ratio $R = 10$ (compression–compression). Subsequent blocks increase the maximal stress by 15 MPa, with a pause between blocks to allow the specimen temperature to return to room temperature (approximately 100 s). This process continues until failure or reaching the phase transformation limit. For the tensile setup, a similar procedure is followed, with the initial maximal stress starting at 80 MPa and increasing in steps of 20 MPa, with a loading ratio of $R = 0.1$ (tension–tension). It is worth noting that the stress remains below the transformation yield stress, keeping the material in the elastic regime and corresponding to HCF.

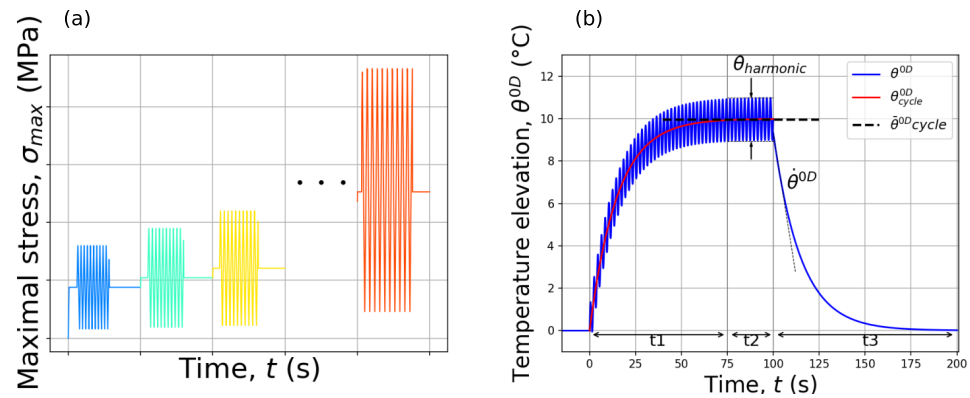


Figure 5. Schematic representation (a) of loading block with maximal stress increasing and loading ratio, $R = 0.1$, and (b) specimen temperature elevation during one stage.

Adopting a zero-dimensional (0D) approach allows for the mean temperature across the gauge length to be considered as the specimen temperature ($T_{specimen}$). This method assumes a uniform temperature distribution. The grip temperatures are representative of the environment temperature. To measure the true specimen temperature evolution, the temperature mean of the upper and lower grips is deducted to $T_{specimen}$. Thus, Equation (1) allows for the determination of the temperature elevation, denoted as θ^{0D} . Notably, the grips are coated in black paint as well. The compression setup uses the same grips used in the compression quasi-static test.

$$\theta^{0D} = T_{specimen} - \frac{T_{uppergrip} + T_{lowergrip}}{2} \quad (1)$$

There exists a different shape of temperature evolution [31]. Generally, the temperature rise reaches a stabilized value after a specific time, as depicted in Figure 5b. This stabilized mean steady state temperature (θ_{cycle}^{0D}) is determined for each loading block. However, the temperature elevations may not stabilize. This behavior possibly indicates the emergence of strain hardening behavior [34]. Consequently, the specimen experiences a non-linear behavior and does not respect the method framework (the self-heating loading needs to stay in the elastic regime of the material). Therefore, only the curves that stabilize will be considered. The thermal signal (θ^{0D}) exhibits oscillations called the first harmonic, which can include thermo-elastic coupling ($\theta_{harmonic}$). It is measured as the average on the maximum and minimum temperature during t_2 . Finally, as the cyclic loading ceases, the temperature elevation cools down and eventually reaches 0 °C before the next loading block. The cooling rate ($\dot{\theta}^{0D}$) when the loading stop can also be reported.

At the moment the cyclic process stops, the thermal source becomes null. Therefore, the cooling rate may be related to the mean steady-state temperature elevation by introducing the characteristic time (τ_{eq}) described by Equation (2). In the 0D approach, τ_{eq} is intricately linked to several factors, including specimen dimensions, material thermal conductivity, and exchange coefficients between the specimen and the grips, as well as between the specimen and the environment. Accurate determination of τ_{eq} entails employing a least squares method to fit Equation (3) to the cooling step during t_3 . This method ensures a robust estimation of the characteristic time, thereby confirms stable thermal dynamics during the cooling phase and overall on the self-heating test itself [29].

$$\dot{\theta}^{0D}(t = t_3) = -\frac{\theta_{cycle}^{0D}}{\tau_{eq}} \quad (2)$$

$$\theta_{cycle}^{0D} = \bar{\theta}_{cycle}^{0D} \times \exp\left(\frac{-t}{\tau_{eq}}\right) \quad (3)$$

The fatigue tests were carried out only on tensile specimens using the exact same setup as the tensile self-heating test. Therefore, the material endurance limit and its stress–numbers of cycles (SN) curves can be determined.

2.4. Microstructure Evolution Preparation

A flat (also called blank) specimen holder was used with Crystalbond Mounting Wax (Buehler, Lake Bluff, IL, USA) to stick the specimens for the grinding and polishing steps with an AutoMet 300 Propolisher (Buehler, Lake Bluff, IL, USA). The mechanical preparation of flat specimens consists of a series of grinding and polishing steps performed with progressively finer abrasive media, ranging from sandpaper foil grade #600 down to 1 μm diamond suspension, to achieve a mirror finish. Because A_f was close to room temperature it is preferable to use warm water for all the cleaning steps to prevent the appearance of martensite [18]. Finally, the specimens undergo a vibratory polishing step using an abrasive colloidal silicate solution (0.08 μm) for 2.5 h at 90 Hz/90% with the QATM Vib machine (Newtown, PA, USA) This final step is not required but strongly recommended and can significantly enhance electron backscatter diffraction (EBSD) analysis, and is suggested to last for at least 2 h [42].

Interrupted fatigue tests were conducted using a Universal Test Resources machine (Shakopee, MN, USA) with a load capacity of 25 kN. These tests were performed at room temperature under load control with a loading ratio $R = 0.1$ and a testing frequency of 20 Hz. Two stress levels were considered: 95 MPa and 160 MPa. Sample 1, referred to as S1, underwent a maximal stress of 95 MPa. However, the specimen did not fail after 1 million cycles. Consequently, the maximal stress was increased to 155 MPa in increments of 15 MPa for a fatigue test of one million cycles at each stage. Sample S1 failed after reaching 155 MPa and underwent a total of 4.365 million cycles, including one million cycles each at stress levels of 95, 110, 125, and 140 MPa and 365,428 cycles at 155 MPa. Sample 2, or S2, failed at 367,151 cycles. For each stress level considered, the fatigue tests were interrupted to perform microstructure observations after several thousand cycles. Table 2 presents all the fatigue interruption points for both samples. In total, each specimen underwent eight interruptions between the initial stage and failure.

Table 2. Fatigue test interruption points for the two specimens.

S1		S2	
Stress	Cycles	Stress	Cycles
	Initial stage		Initial stage
95 MPa	100 k; 300 k; 600 k; 1 M	160 MPa	10 k; 20 k; 30 k;
110 MPa	1 M		50 k; 80 k; 120 k;
125 MPa	1 M		180 k; 367 k → Failure
140 MPa	1 M		
155 MPa	365 k → Failure		

On each specimen, two zones, Z1 and Z2, measuring $360 \mu\text{m} \times 360 \mu\text{m}$, were selected for EBSD analysis using an Oxford Instrument Symmetry S2 (High Wycombe, UK) and SEM imaging with an FEI Quanta FEG (Hillsboro, OR, USA), both initially and at every interruption step. A sub-micron step size of 0.9 μm was chosen for the analysis. In addition, an optical microscope Keyence VHX-500 (Itasca, IL, USA) using polarized light was employed to capture images and topology of the surface with a resolution of 0.4 μm . Figure 6 provides the precise localization of the observed zones. Zone 1 is between the fillet and the centre of the gauge length. Zone 2 is in the middle of the gauge length. After failure, additional EBSD results were obtained both before and after a thermal flash up to 80 $^{\circ}\text{C}$ for a few seconds and cooling down with the same parameters. These analyses were conducted at higher magnification and a smaller step size.

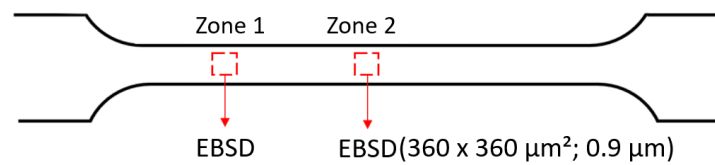


Figure 6. Schematic representation of one specimen and its two observed zones.

Finally, one of the most challenging aspects of this process is maintaining the integrity of the specimen observed surface throughout, given the numerous loading and unloading cycles involved in both the fatigue test bench and the SEM.

3. Self-Heating Assessment

3.1. Cyclic Compression Loading

The thermal signal of Specimen 1 from Batch 1 can be plotted for each stress level, as illustrated in Figure 7a. The temperature elevation aligns with previous theoretical descriptions for each stress level, revealing several insights. Notably, dissipation increases with maximal stress. However, the temperature elevation remains relatively low, even at high stress levels, compared to previous studies utilizing the self-heating test [28]. This correlation with the solicited volume was anticipated due to the small geometry utilized in this study. In all the curves, the temperature evolution does not evolve more than 1%, so every loading block is considered in the followings analysis.

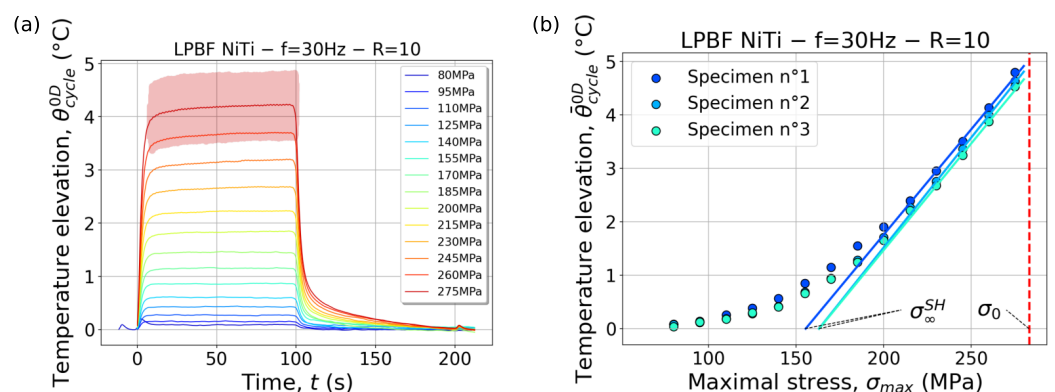


Figure 7. (a) Mean temperature elevation under cyclic loading at different stress level of Specimen 1— Batch 1. The value of θ^{0D} is shown only for t_2 and on the loading block at 275 MPa for the sake of clarity. (b) Repeated self-heating curves of LPBF-NiTi with $R = 10$. The blue lines are linear regressions on the last three points of each curve and show the empirical fatigue limit at the intersection with the x-axis. The red dotted line shows the transformation limit.

The stabilized mean steady-state temperature versus the corresponding maximal stress for each block, commonly known as the self-heating curve, is depicted in Figure 7b. This method was repeated at least three times to ensure the test repeatability. Analysis of these self-heating curves reveals that the mean steady-state temperature elevation increases with maximal stress, ranging from 0.2 °C to 4.78 °C for stresses of 80 MPa and 275 MPa, respectively. This indicates an increase in the number of dissipative mechanisms with higher stress levels. Utilizing the method proposed by [27], the empirical fatigue limit (σ_{∞}^{SH}) is determined at the intersection between the maximal stress axis (x-axis) and the linear regression of the last three points on the curve. As a result, empirical fatigue limits of 155 MPa, 163 MPa, and 163 MPa are determined for the repeated tests, indicating acceptable test repeatability.

Figure 8 illustrates the average amplitude of the first harmonic at each stress level. Two distinct regimes are observed in each specimen. In the lower stress range from 80 to 220 MPa, the coupling exhibits a linear increasing trend with a consistent slope of 2.75×10^{-3} °C/MPa. However, beyond 240 MPa, the amplitude of the first harmonic

increases significantly faster, with a slope above 3.31×10^{-2} and $2.77 \times 10^{-2} \text{ } ^\circ\text{C}/\text{MPa}$, for Specimen 1 and the average of Specimens 2 and 3. The significant change between both regimes represents an order of magnitude difference. The initial regime can be attributed to thermoelastic coupling occurring during the loading blocks, with the amplitude of coupling increasing proportionally to the stress level. Subsequently, the emergence of the second regime signifies a notable shift in material behavior, potentially indicating the initiation of phase transformation at a micro scale. Nevertheless, the mean steady-state temperature was constant during the loading block, indicating that the transformation is not generalized, and the sample remains global in its elastic behavior.

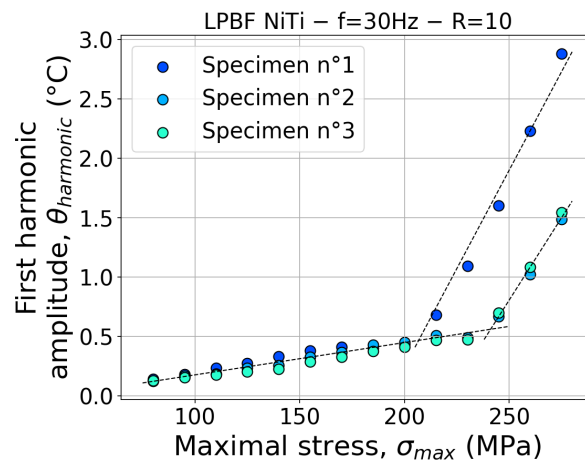


Figure 8. Amplitude of the first harmonic of each loading block of specimens from Batch 1. The dotted lines are the linear regressions of both regimes where the slopes were measured.

The self-heating method offers a rapid means to empirically determine the fatigue limit of a material, requiring only a single test. Additionally, it potentially describes phase transformation occurrences under cyclic loading conditions. However, to validate its reliability, empirical fatigue limits must be compared with conventional fatigue test results. Despite conducting fatigue tests with a loading ratio of $R = 10$, no failures were observed, consistent with expectations based on existing literature [43]. Therefore, to enable a comparison between self-heating and fatigue results, the method was extended to include a tensile setup.

3.2. Cyclic Tensile Loading

The identical methodology was applied to conduct tensile self-heating tests using specimens from Batch 2. Each specimen experienced failure during the 320 MPa loading blocks. Figure 9a depicts the temperature elevation for each loading block of Specimen 1, along with the self-heating curves of three specimens. In contrast to the compression tests, the temperature elevation did not stabilize during the final 1000 cycles of the last loading block at high stress levels. For instance, as illustrated in Figure 9a, the mean temperature elevation decreased by 2.5%, 1.91%, and 0.5% for stress levels of 300, 280, and 260 MPa, respectively. Given that the evolution exceeded 1%, the last two stress levels were excluded from the self-heating curve. Self-heating curves in Figure 9b indicate an increase in mean steady-state temperature elevation with maximal stress levels as expected from self-heating tests. The temperature elevation ranged from 0.18 $^\circ\text{C}$ at 80 MPa to 7.24 $^\circ\text{C}$ at 260 MPa. Based on empirical determinations, endurance limits of 149, 150, and 153 MPa were identified for the repeated tests. Notably, the repeatability of the results was significant, with a difference of 10.3 MPa observed between the average values of the empirical endurance limits for both loading types.

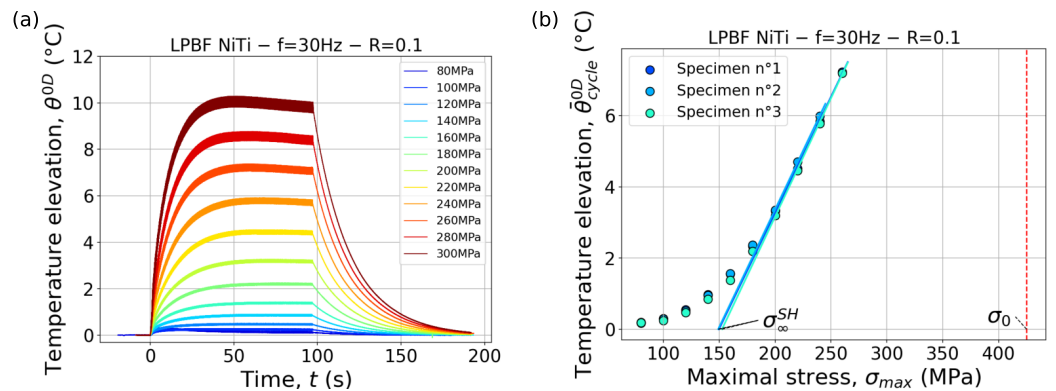


Figure 9. (a) Temperature elevation under cyclic loading at different stress level of Specimen 1—Batch 2. (b) Repeated self-heating curves of LPBF-NiTi with $R = 0.1$. The blue lines are linear regressions on the last three points of each curve and show the empirical fatigue limit at the intersection with the x-axis. The red dotted line shows the transformation limit.

Similar to Batch 1, an investigation into the amplitude of the first harmonic was undertaken. Figure 10a illustrates the evolution of the first harmonic amplitude. Once again, two distinct regimes were discerned: an initial linear trend spanning from 80 to 165 MPa, wherein the amplitude increased from 0.06 to 0.13 °C with an average slope of 4.58×10^{-4} °C/MPa. It is followed by a pronounced increase in slope up to 4.37×10^{-3} °C/MPa, where the amplitude peaked at 0.47 °C. This pattern closely resembles that observed in the compression tests, two linear regime with an increase of an order of magnitude.

This behavior is additional evidence to consider is the hypothesis that micro phase transformation occurs during loading. However, this hypothesis may be subject to debate, particularly considering that the stress level of 165 MPa is lower than the macroscopic phase transformation limit measured at 425 MPa in a quasi-static test. Further analyses may be required; for instance, DIC measurement along a self-heating test could confirm the linear behavior of the material. Nevertheless, the heterogeneities induced by the LPBF process can potentially introduce stress concentration and lead to such behavior on a local scale.

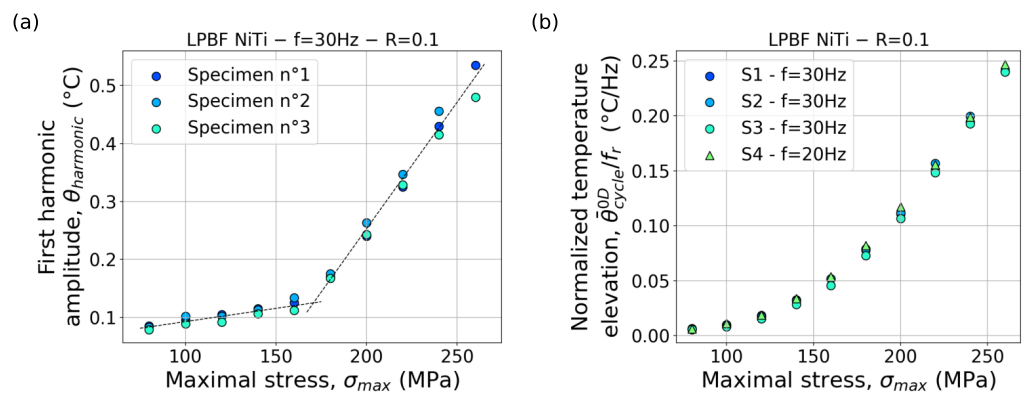


Figure 10. (a) Amplitude of the first harmonic of each loading block of specimens from Batch 2. (b) Self-heating curves comparison with two different frequencies of 20 and 30 Hz.

In the thermal measurement of cyclic loading, frequency emerges as a significant parameter influencing material dissipation [44]. Thus, it becomes imperative to examine the effect of frequency on self-heating tests. For this purpose, two distinct frequencies, 20 and 30 Hz, were considered. In Figure 10b, the curves are normalized by dividing the mean steady-state temperature by the frequency. Notably, the self-heating curves for both frequencies exhibit similar behavior. Consequently, the evolution of temperature elevations can be regarded as a linear function of frequency. This behavior aligns with findings in previous studies [28,29], indicating a consistent intrinsic dissipation of the

material. Therefore, there is no necessity to repeat the self-heating method at different frequencies to assess the empirical endurance limit.

After fitting Equation (3) on the self-heating curves for all specimens, the values of τ_{eq} exhibit constancy across each stress level, averaging approximately 21.4 ± 0.8 s. Figure 11 compares the terms of Equation (2) to corroborate the identification of the characteristic time. Results obtained from all three specimens and both methods demonstrate good agreement, affirming the correct thermal test conditions. The potential occurrence of phase transformation, inferred from the increase in first harmonic amplitude after 165 MPa, is likely localized and does not significantly alter the thermal conditions. Consequently, we may confirm that the material stays in this elastic regime even at higher stress.

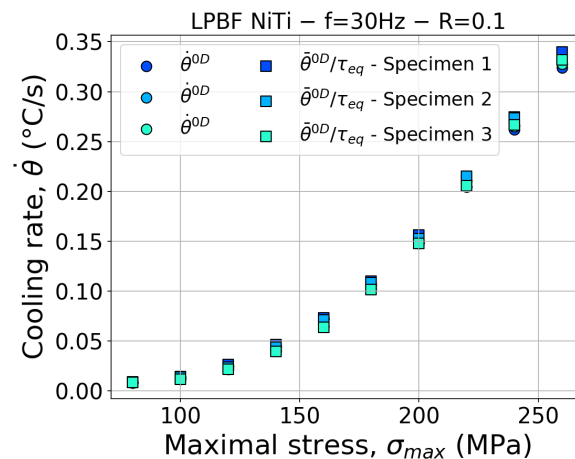


Figure 11. Comparison of SH curves with two different methods.

After assessing the self-heating behavior of LPBF-NiTi in both compression and tension, it is imperative to compare the empirically determined endurance limit with classic fatigue results.

4. Fatigue Assessment

4.1. Fatigue Results

The classic fatigue tests were carried out with the same batch of tensile specimens (Batch 2) and testing machine as the self-heating test. The loading parameters are identical, also: frequency $f_r = 30$ Hz, a loading ratio $R = 0.1$. Figure 12 shows the S-N curve plotted with 15 fatigue tests. The specimens that did not fail after 1 million cycles are represented by an arrow. The endurance limit (σ_{∞}^{fat}) obtained with the fatigue tests was determined at 111 MPa. A difference with the endurance limit determined with the self-heating method is observed. The link between the fatigue and the self-heating behavior is not obvious. Therefore, caution should be exercised when drawing conclusions about the correlation between self-heating and HCF.

It is widely acknowledged that LPBF and other AM processes introduce internal defects in fabricated parts, even when process parameters are optimized [45]. These defects act as stress concentrators and can lead to premature fatigue failure [24,46]. Therefore, SEM imaging was conducted on the fracture surfaces of specimens subjected to fatigue tests. Figure 13 displays two SEM images of fracture surfaces from specimens that failed after 101,063 cycles (a) and 332,406 cycles (b). The crack initiations are visibly located near the surface, indicated by the red circles. Surface and subsurface defects are discernible, although determining their exact nature proves challenging. Additionally, Figure 13b depicts a failure profile resembling a step, indicative of two distinct crack initiations. Notably, these crack initiations are situated on the same side of the specimen that was in contact with the support structure. Previous studies, such as [25], have highlighted that even after support structure extraction and manual polishing, residual defects near the surface can still trigger premature fatigue failure. Additionally, several crack initiations

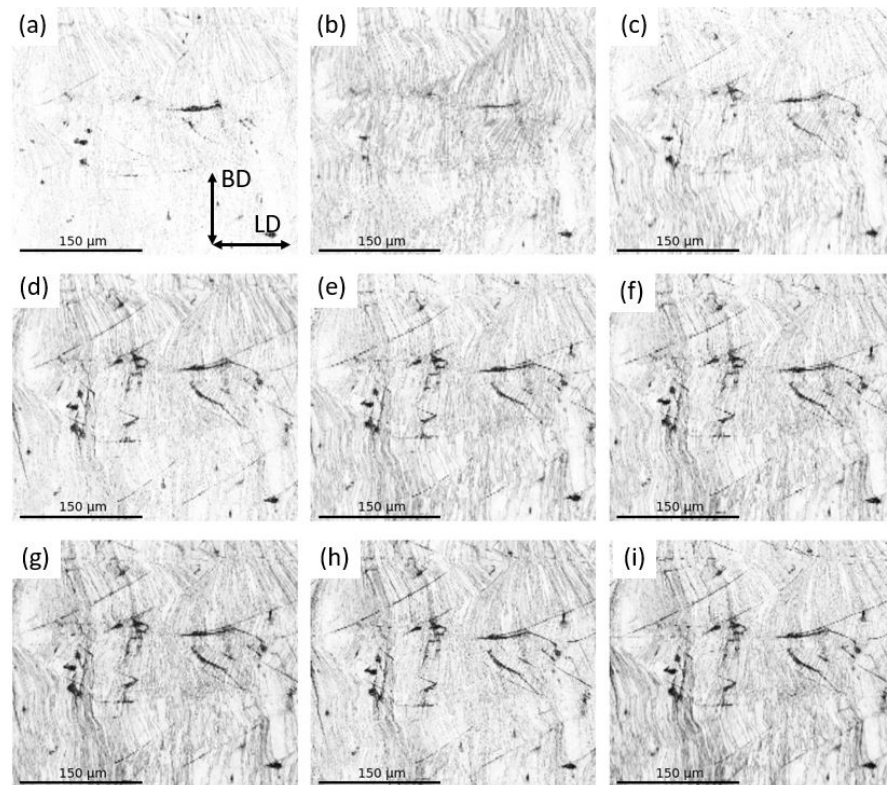


Figure 14. Band contrast of S1-Z1 at different stages of cycling: (a) initial stage; at 95 MPa after applying (b) 100,000 cycles; (c) 300,000 cycles; (d) 600,000 cycles; (e) 1,000,000 cycles; (f) after applying 1,000,000 cycles at 110 MPa; (g) after applying 1,000,000 cycles at 125 MPa; (h) after applying 1,000,000 cycles at 140 MPa; (i) after applying 365,428 cycles at 155 MPa. BD: bulging direction; LD: loading direction.

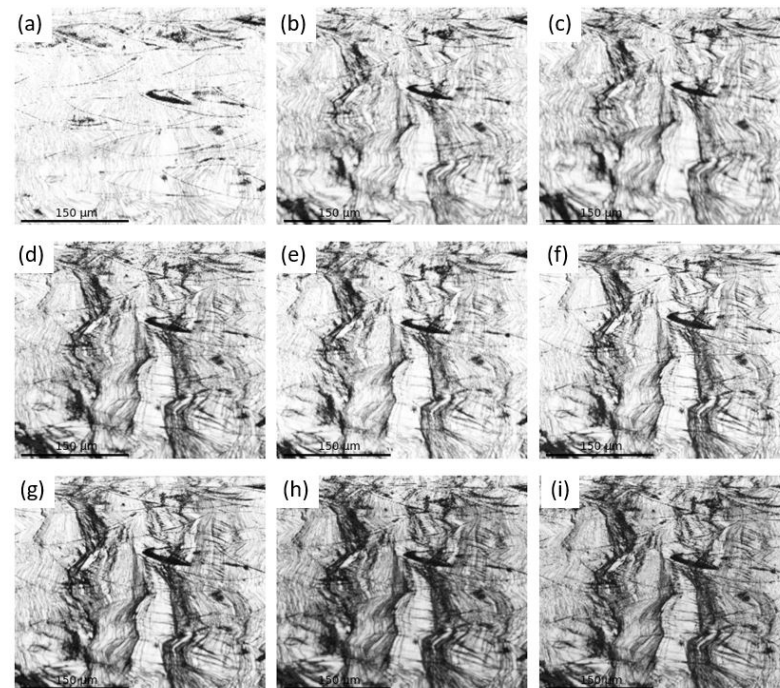


Figure 15. Band contrast of S2-Z1 at different stages of cycling at 160 MPa: (a) initial stage; after applying (b) 10,000 cycles; (c) 20,000 cycles; (d) 30,000 cycles; (e) 50,000 cycles; (f) 80,000 cycles; (g) 120,000 cycles; (h) 180,000 cycles; (i) 367,151 cycles.

Once the 95 MPa loading started on S1, an evolution of the mechanisms is observed, including the growth of existing regions from the initial stage and the appearance of new ones along melt pool boundaries and random locations from 0 to 1 million cycles (Figure 14a–e). After reaching 1 million cycles, the stress increased, and the results after 1 million cycles were documented (Figure 14f–i). The evolution appeared to continue progressing, with no apparent influence from the building direction or loading direction. On S2, the evolution was much more pronounced upon loading initiation due to higher applied stress (Figure 15b–i). Here, the appearance and growth of non-indexed regions were mainly aligned with the building direction with a zig-zag shape following the grain boundaries. Most of these regions exhibited an angle between 45° and 90° with the loading direction, which is considered the most critical angle for plastic slip or phase transformation [53,54]. Additionally, some locations appeared less impacted, indicating a more pronounced growth compared to the appearance of new regions. Overall the observed evolution can be quantified.

To undertake a quantitative assessment of these phenomena, a specific methodology was adopted to measure the areas influenced by these mechanisms within the observations. This approach leverages a binary technique reliant on gray level thresholding and detection size criteria, accounting for contrast color and the minimum pixel count requisite for defining a mechanism, as depicted in Figure 16. The criteria set for this analysis included a 40% contrast threshold and a 4-pixel minimum for feature identification, with an allowable contrast error margin of $\pm 5\%$. This binary method has been effectively applied in prior studies for the quantitative analysis of persistent slip bands (PSBs) and the exclusion of misorientation measurements related to grain and melt pool boundaries [31].

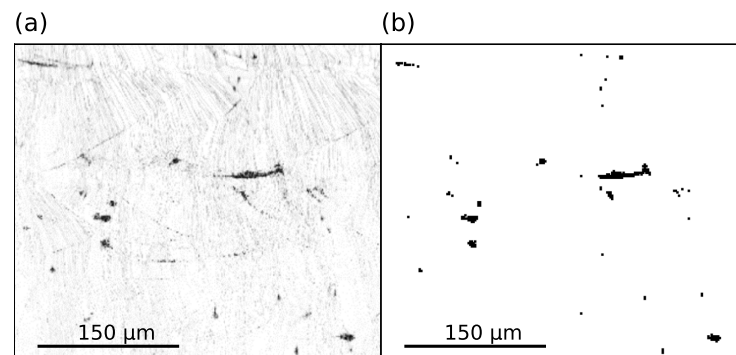


Figure 16. Example of mechanism detection result of the binary process on S1-Z1 (Figure 14a): (a) initial images, (b) image after applying the binary process.

Figure 17 presents the ratio of areas impacted by non-indexed regions against the total analyzed area for each specimen, each measuring 360 μm by 360 μm . For zone S1-Z1, the initial one million cycles under a 95 MPa load showcase a modest increase in the prevalence of mechanisms, from 0.62% to 1.41%. With further loading, the magnitude of this evolution accentuates, culminating in 4.46% at the point of failure. In contrast, specimen S1-Z2, subjected to identical loading conditions, exhibits no marked progression in mechanism development within the margin of error. For Specimen 2, the escalation in both the frequency and dimensions of these mechanisms is significantly more pronounced than in Specimen 1. This upward trend correlates directly with the higher stress level, achieving peaks of 20.70% and 10.43% for zones S2-Z1 and S2-Z2, respectively, illustrating a distinct pattern in the response to cyclic loading.

The level of applied stress significantly influences the emergence and growth of mechanisms. Below a critical stress threshold of 110 MPa, changes remain negligible; yet, surpassing this threshold triggers an evident evolution, where increased stress levels correspond to a more rapid rate of mechanism evolution. Distinct responses were noted across the zones, with Zone 1 showing a more extensive area of effect than Zone 2. To clarify these divergent patterns, additional comprehensive studies are warranted. The presence of

outliers may be ascribed to the challenges inherent in the EBSD setup, which includes maintaining consistent observation angles and exact locations across measurements, particularly noticeable at 160 MPa– 30 k cycles in S2-Z2.

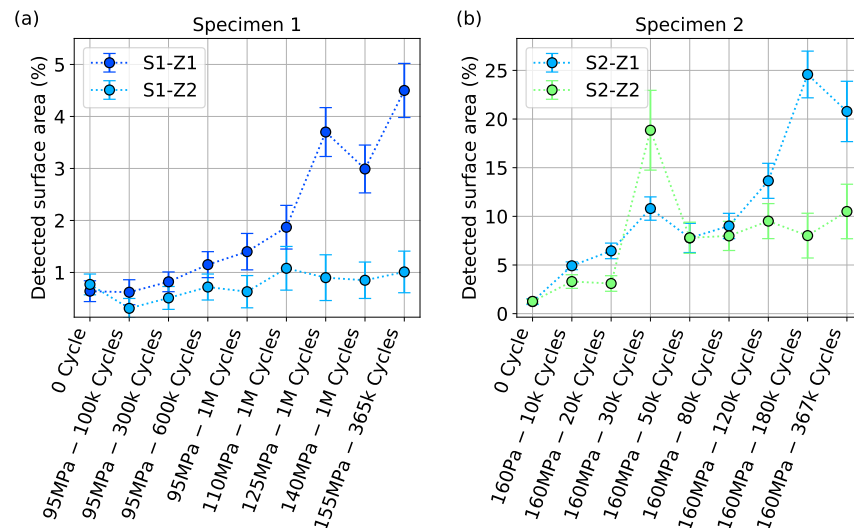


Figure 17. Evolution of non- and poor-indexed EBSD indexation area of (a) S1 and (b) S2.

The Euler angles maps presented in Figure 18 reveal distinct microstructural characteristics in the selected zones. S1-Z1 and S2-Z1 exhibit large areas (>100 μm) where the colors are very close, despite the grains being reported to be finer in these locations with the band contrast result. Most of the grains display very similar crystal orientations in these areas. However, at interfaces between different colors (see arrows in Figure 18a,c), significant disorientation is observed. These interfaces coincide with the locations of most features, suggesting that this microstructure is more prone to the initiation of mechanisms. Once the mechanisms appear at the interface, growth continues along the interfaces. In contrast, S1-Z2 and S2-Z2 do not exhibit large areas with the same Euler angles. Both zones consist of numerous smaller areas with different crystal orientation. Therefore, although the initiation of mechanisms is not limited, growth may be constrained. These results confirm the difference in behavior between Z1 and Z2 for both specimens, probably due to the variability in LPBF material, especially near the surface [55].

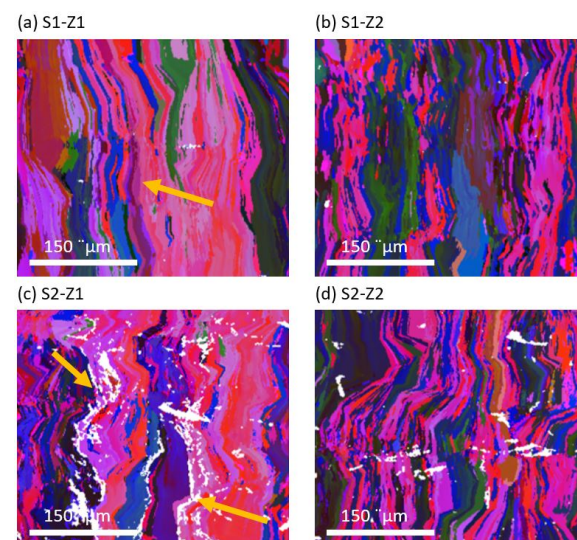


Figure 18. Euler angle maps of the different location at the failure stage of both specimens: (a) S1-Z1; (b) S1-Z2; (c) S2-Z1; (d) S2-Z2. Arrows highlight the significant crystal misorientation interfaces.

4.3. Mechanisms Identification

Inverse pole figures (IPFs) are used to detail the crystallographic orientation of grains relative to a specific reference direction. The IPF map, depicted in Figure 19, reveals a fine-grained microstructure with columnar grains oriented along the build direction, as confirmed by band contrast analysis. This examination also uncovers a pronounced $\langle 001 \rangle$ crystallographic texture. When integrating band contrast data with the IPF map, no irregular features are observed at specific grain boundary regions. Further inspection of the IPF map enables the differentiation between two types of boundaries based on crystal misorientation criteria: any point pair showing misorientation greater than 2° is deemed a boundary. Specifically, misorientations over 10° define grain boundaries, whereas those in the 2° to 10° range indicate internal grain misorientations. Intra-grain misorientations are marked by white lines with arrows, and grain boundaries are marked by black lines. The kernel average misorientation (KAM) maps, particularly in Figure 19c, highlight intra-grain misorientation with green-yellow coloring, pinpointing the presence of intra-grain boundaries. Despite the presence of fine columnar grains, internal misorientations are observed, likely arising from the remelting process [56,57].

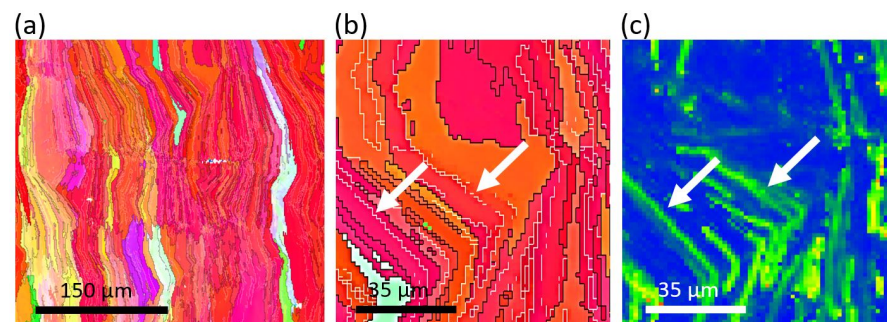


Figure 19. IPF-Y, and grain boundaries maps of (a) S1-Z1, (b) a zoom in the first image, (c) the corresponding KAM map. Arrows show the location of intra grain misorientation on the IPF and KAM maps.

The study extends beyond microstructural evolution, as depicted through band contrast maps, to include an analysis of crystal misorientation, grounded in predefined boundaries that align with KAM results. Due to the small grains, it is challenging to clearly identify internal grain misorientation. Therefore, the quantity of boundaries in the map can be measured. The internal boundaries ($<10^\circ$) and grain boundaries ($>10^\circ$) are discriminated across all interrupted stages of the analysis. Figure 20 illustrates the evolution of intra-grain boundary proportions in the different zones. This approach offers a nuanced view of the microstructural changes, highlighting the dynamics of intra-grain boundary development throughout the process.

To ensure uniform stress levels during the analysis, only stress magnitudes of 95 MPa and 160 MPa were examined. Within S1, an increase in intra-grain misorientation was noted across both zones, contrasting with the observed feature evolution trends. Despite differing initial intra-grain misorientation ratios, an approximate 2% increase was recorded from the initial stage to the one million cycle mark in both zones. S2 mirrored S1 in initial proportions and cyclic loading responses, with intra-grain misorientation rising up to 6% in S2-Z1 and 4% in S2-Z2. One outlier data point is reported at the 30k cycle in S2-Z2, aligning with the band contrast analysis findings. The investigation underscores the impact of applied stress on intra-grain misorientation across the studied zones, even at the relatively low stress level of 95 MPa. This is contrasted with the evolution of feature populations discernible through band contrast, which exhibited significant changes beginning at a stress threshold of 110 MPa. The primary mechanism unveiled in this research is internal microplasticity, observable at lower stress levels and further accentuated under increased stress.

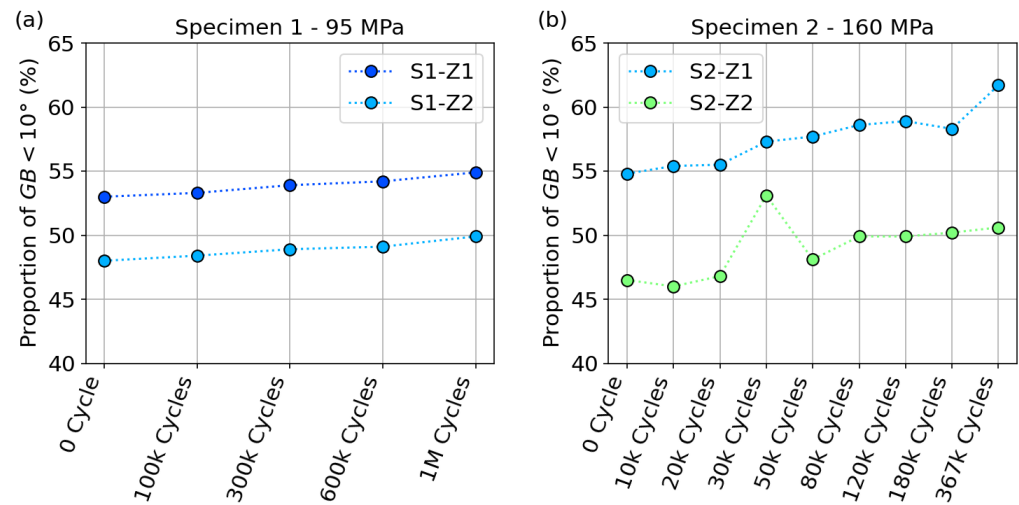


Figure 20. Evolution of proportion of the intra-grain boundaries in (a) Specimen 1 and (b) Specimen 2.

It is well reported in the literature that in the HCF regime in a conventional alloy, dislocations pile-ups and PSBs are the predominant mechanisms and can lead to extrusion of planes at the surface of ductile materials and eventually to crack initiation and, ultimately, fatigue failure [58–60]. However, nobody has claimed to observed this type of mechanism in NiTi alloys. To assert that these types of plastic defects are the observed mechanisms in this work, an examination of the surface morphology is required [49]. SEM images were captured at the initial stage, and after failure on Zone 1 for both specimens (Figure 21). It is clear that loading induced topological changes in both specimens due to the surface extrusion and, more significantly, in S2 with higher stress. These changes appeared to occur predominantly in the non-indexed zones reported previously, but not exclusively. These surface extrusions can be measured and clearly identify the types of mechanisms.

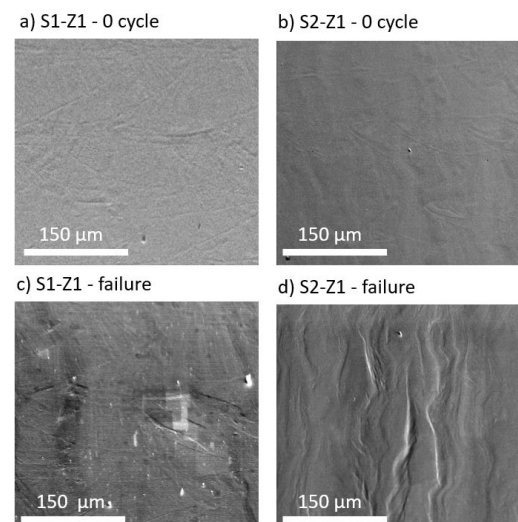


Figure 21. SEM images of Zone 1 at the initial stage of (a) S1 and (b) S2, and after the failure of (c) S1 and (d) S2.

Furthermore, optical microscope analysis captured height profiles, and the results for S2-Z1 are presented in Figure 22. Three profiles were measured on the surface of S2-Z1 that were the most impacted area by the mechanisms. Profile 1 goes along a region where mechanisms were detected with a binary process. A significant step was measured with a height extrusion of 7.22 μm, and the step width is 70 μm. Similar results are present with the Profiles 2 and 3 with a 6.86 and 5.50 μm height. These values are in the range on PSBs in the literature under HCF loading [61–65]. When comparing the grain orientation, it does

not appear that specific crystal orientation promotes the phenomenon. Thus, a second mechanism of surface extrusion due to accumulation of PSBs is identified and occurs at higher stress level.

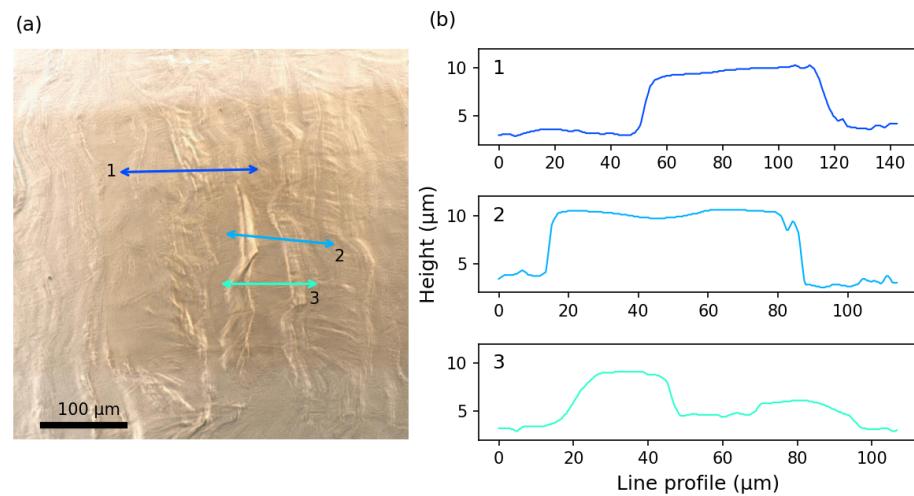


Figure 22. (a) Optical image from S2-Z1 with polarized light. (b) Three profiles measuring heights on different location represented with arrows on the image.

Once the failure occurs, the thermal flash is applied to each specimen. Typically, such thermal flash following mechanical loading can aid shape memory alloys in recovering a fraction or completely reversing residual strain through the reverse transformation of retained martensite, which can be blocked by defects [66,67]. With this thermal flash, some surface features vanished according to the binary process depicted in Figure 23. Therefore, the possibility that a proportion of the mechanisms represents strain-induced martensite is promising and in agreement with the decrease of the area fraction of mechanisms on band contrast.

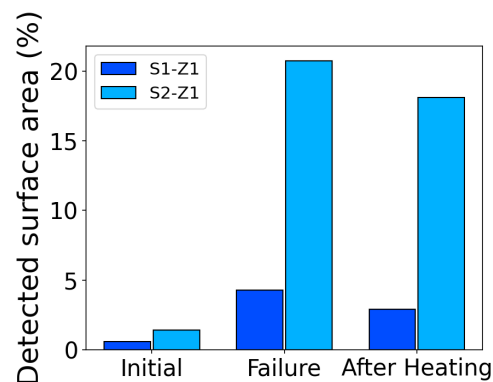


Figure 23. Evolution of the mechanism area at the initial stage, the failure stage, and after the thermal flash.

To verify this claim, higher magnification images and smaller EBSD step size maps were obtained and are presented in Figure 24. Upon loading, some surface features appeared and even tended to grow with the number of cycles, leading to “canyon” shape features (see Figure 24a). Phase identification indexed austenite away from these features. Some data points indexed martensite on the features, but not on the complete shape. The fine structure of martensite may have dimensions smaller than 100 nm, which could account for the incomplete indexing of the shapes. Moreover, due to changes in surface topology, obtaining EBSD Kikuchi bands for phase analysis may not be optimal. No specific grain orientations appear to predispose the appearance of stress-induced martensite (SIM). Additionally, these mechanisms do not exclusively manifest at grain or melt pool

boundaries. Figure 24b illustrates the same location after heating. Although a fraction of martensite persisted, the majority transformed back into the austenite phase. This outcome validates the occurrence of martensite formation during cycling, despite the maximum stress remaining within the elastic regime due to stress concentration induced by defects such as slip bands and dislocations [65,68]. Under elastic loading, no macroscopic phase transformation occurs. However, grains experiencing stress concentration due to localized defects may undergo shear stress, eventually triggering phase transformation upon reaching the phase transformation limit. It appears that this type of mechanism is not dictated by grain orientation. These results are evidence that the micro-phase transformation occurs under HCF loading and can be captured with the analysis on the change in the behavior of the amplitude of the first harmonic.

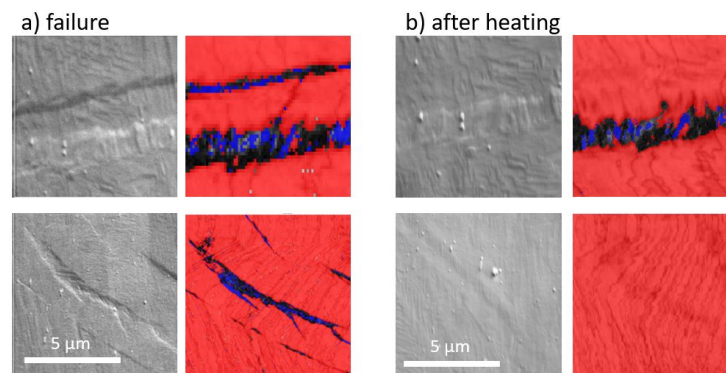


Figure 24. SEM images of S1-Z1 at a magnification of $\times 5000$ and phase identification map with a step size of $0.1\mu\text{m}$ for two surface features: (a) at the failure stage and (b) after the thermal flash. The red and blue colors correspond to austenite and martensite phases, respectively.

The final investigation focuses on the mechanism that led to the failure. Figure 25 shows the Euler maps at the failure for both specimens. In both cases, the Euler maps exhibit the same type of microstructure as S1-Z2 and S2-Z2, characterized by a multitude of crystal orientations not favorable for the appearance and propagation of the observed mechanism. Additionally, SEM images of the failed surface display characteristic HCF failure [69]. A zoom at the crack initiation reveals surface or sub-surface defects of approximately $40\mu\text{m}$, which are the origin of the failure. These defects exhibit typical shapes of lack of fusion, and their location near the surface makes them more critical in fatigue. Therefore, the fatigue properties of LPBF-NiTi are more likely driven by the inherent process induced defect. However, the cracks propagate along the grain boundaries, where the mechanisms were identified to facilitate the crack propagation.

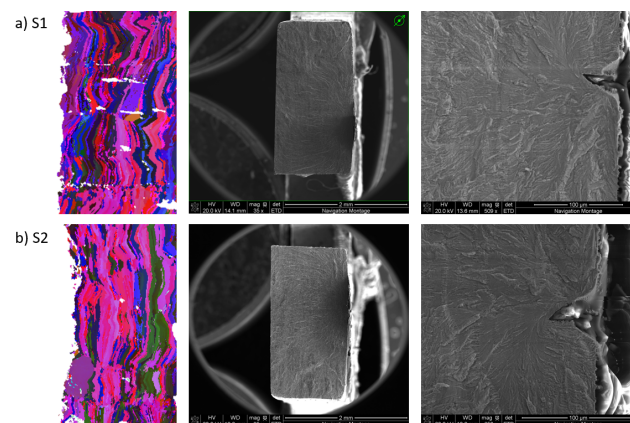


Figure 25. Euler maps for the failure and SEM images of the failed surface for (a) Specimen 1 and (b) Specimen 2.

5. Conclusions and Perspectives

The aim of this work was to characterize the self-heating behavior of LPBF-NiTi under two different loading modes and to investigate its HCF properties and associated mechanisms. From the study, several conclusions and perspectives emerge:

- The self-heating behavior of LPBF-NiTi was investigated for the first time, revealing relatively similar results regardless of the loading ratio. It was observed that, with the selected frequency and when the maximum stress remained lower than the phase transformation limit, micro-phase transformation at lower scale may occur at stress levels from 240 MPa in compression and 165 MPa in tension, inducing the increase in the amplitude of the first harmonic.
- The self-heating method demonstrated a consistency in repeated tests. The endurance limit at 1 million cycles was reported empirically at 150 MPa in tensile loading. This value was compared to the value obtained from classical fatigue results, revealing a significant discrepancy. Consequently, any conclusions drawn about the relationship between self-heating and HCF should be approached with caution.
- Three mechanisms induced by HCF loading were identified. At lower stress levels, a microplasticity mechanism within the grains, associated with intra-grain misorientation, was observed. At higher stress levels, the predominant mechanism is surface extrusion, resulting from the accumulation of dislocations and persistent slip bands on the surface, which is also attributed to microplasticity. These two mechanisms, occurring at different stress levels, are similar to those observed in traditional materials. In the context of shape memory features, stress-induced martensite can be stabilized under HCF loading, albeit in smaller quantities. Although the study could not clearly quantify these mechanisms, further statistical analysis could provide meaningful insights.
- Both HCF and self-heating loading were carried out in the elastic regime of the material. These observations can be used to support the hypothesis toward the self-heating modeling.
- The presence of defects near the surface in the material is more likely the origin of crack initiation. The crack propagation occurs along the grain boundaries and is facilitated by plastic mechanisms, leading to fatigue failure.

Author Contributions: Conceptualization, T.C. and S.A.C.; Data curation, T.C.; Formal analysis, T.C.; Investigation, T.C.; Methodology, T.C. and S.A.C.; Project administration, S.A.C.; Resources, T.C., M.E. and S.A.C.; Supervision, L.S.-S., M.E. and S.A.C.; Visualization, T.C.; Writing—original draft, T.C.; Writing—review and editing, T.C., L.S.-S. and S.A.C. All authors have read and agreed to the published version of the manuscript.

Funding: This research received no external funding.

Data Availability Statement: The raw data supporting the conclusions of this article will be made available by the authors on request.

Acknowledgments: The study was supported by the European Commission through the CPER DURABIMAT EU000902.

Conflicts of Interest: The authors declare no conflicts of interest.

References

1. Mohd Jani, J.; Leary, M.; Subic, A.; Gibson, M.A. A review of shape memory alloy research, applications and opportunities. *Mater. Des.* **2014**, *56*, 1078–1113. [[CrossRef](#)]
2. Elahinia, M.; Shayesteh Moghaddam, N.; Taheri Andani, M.; Amerinatanzi, A.; Bimber, B.A.; Hamilton, R.F. Fabrication of NiTi through additive manufacturing: A review. *Prog. Mater. Sci.* **2016**, *83*, 630–663. [[CrossRef](#)]
3. Ruth, D.J.S.; Sohn, J.W.; Dhanalakshmi, K.; Choi, S.B. Control Aspects of Shape Memory Alloys in Robotics Applications: A Review over the Last Decade. *Sensors* **2022**, *22*, 4860. [[CrossRef](#)]
4. Chau, E.T.F.; Friend, C.M.; Allen, D.M.; Hora, J.; Webster, J.R. A technical and economic appraisal of shape memory alloys for aerospace applications. *Mater. Sci. Eng. A* **2006**, *438–440*, 589–592. [[CrossRef](#)]
5. Stoeckel, D. Shape memory actuators for automotive applications. *Mater. Des.* **1990**, *11*, 302–307. [[CrossRef](#)]

6. Mantovani, D. Shape memory alloys: Properties and biomedical applications. *JOM* **2000**, *52*, 36–44. [[CrossRef](#)]
7. Gheorghita, V.; Gumpel, P.; Strittmatter, J.; Anghel, C.; Heitz, T.; Senn, M. Using Shape Memory Alloys in Automotive Safety Systems. In *Proceedings of the FISITA 2012 World Automotive Congress (Beijing, China, November 2012)*; Lecture Notes in Electrical Engineering; Springer: Berlin/Heidelberg, Germany, 2013; pp. 909–917. [[CrossRef](#)]
8. Elahinia, M.; Shayesteh Moghaddam, N.; Amerinatanzi, A.; Saedi, S.; Toker, G.P.; Karaca, H.; Bigelow, G.S.; Benafan, O. Additive manufacturing of NiTiHf high temperature shape memory alloy. *Scr. Mater.* **2018**, *145*, 90–94. [[CrossRef](#)]
9. Sabahi, N.; Chen, W.; Wang, C.H.; Kruzic, J.J.; Li, X. A Review on Additive Manufacturing of Shape-Memory Materials for Biomedical Applications. *JOM* **2020**, *72*, 1229–1253. [[CrossRef](#)]
10. Muntasir Billah, A.; Rahman, J.; Zhang, Q. Shape memory alloys (SMAs) for resilient bridges: A state-of-the-art review. *Structures* **2022**, *37*, 514–527. [[CrossRef](#)]
11. Chen, J.; Lei, L.; Fang, G. Elastocaloric cooling of shape memory alloys: A review. *Mater. Today Commun.* **2021**, *28*, 102706. [[CrossRef](#)]
12. Nair, V.S.; Nachimuthu, R. The role of NiTi shape memory alloys in quality of life improvement through medical advancements: A comprehensive review. *Proc. Inst. Mech. Eng. Part H J. Eng. Med.* **2022**, *236*, 923–950. [[CrossRef](#)] [[PubMed](#)]
13. Buehler, W.J.; Gilfrich, J.V.; Wiley, R.C. Effect of Low-Temperature Phase Changes on the Mechanical Properties of Alloys near Composition TiNi. *J. Appl. Phys.* **1963**, *34*, 1475–1477. [[CrossRef](#)]
14. Chowdhury, P.; Sehitoglu, H. Deformation physics of shape memory alloys—Fundamentals at atomistic frontier. *Prog. Mater. Sci.* **2017**, *88*, 49–88. [[CrossRef](#)]
15. Kordizadeh, F.; Safaei, K.; Mohajerani, S.; Elahinia, M. Investigation of the elastocaloric effect in laser powder bed fusion NiTi porous structures. *Addit. Manuf. Lett.* **2023**, *6*, 100131. [[CrossRef](#)]
16. Safaei, K.; Nematollahi, M.; Bayati, P.; Kordizadeh, F.; Andani, M.T.; Abedi, H.; Poorganji, B.; Elahinia, M. On the crystallographic texture and torsional behavior of NiTi shape memory alloy processed by laser powder bed fusion: Effect of build orientation. *Addit. Manuf.* **2022**, *59*, 103184. [[CrossRef](#)]
17. Zhu, J.N.; Liu, K.; Riemsagel, T.; Tichelaar, F.D.; Borisov, E.; Yao, X.; Popovich, A.; Huizenga, R.; Hermans, M.; Popovich, V. Achieving superelasticity in additively manufactured Ni-lean NiTi by crystallographic design. *Mater. Des.* **2023**, *230*, 111949. [[CrossRef](#)]
18. Bassani, P.; Fiocchi, J.; Tuissi, A.; Biffi, C.A. Investigation of the Effect of Laser Fluence on Microstructure and Martensitic Transformation for Realizing Functionally Graded NiTi Shape Memory Alloy via Laser Powder Bed Fusion. *Appl. Sci.* **2023**, *13*, 882. [[CrossRef](#)]
19. Nematollahi, M.; Safaei, K.; Bayati, P.; Elahinia, M. Functionally graded NiTi shape memory alloy: Selective laser melting fabrication and multi-scale characterization. *Mater. Lett.* **2021**, *292*, 129648. [[CrossRef](#)]
20. Eggeler, G.; Hornbogen, E.; Yawny, A.; Heckmann, A.; Wagner, M. Structural and functional fatigue of NiTi shape memory alloys. *Mater. Sci. Eng. A* **2004**, *378*, 24–33. [[CrossRef](#)]
21. Mahtabi, M.J.; Shamsaei, N.; Mitchell, M.R. Fatigue of Nitinol: The state-of-the-art and ongoing challenges. *J. Mech. Behav. Biomed. Mater.* **2015**, *50*, 228–254. [[CrossRef](#)]
22. Speirs, M.; Van Hooreweder, B.; Van Humbeeck, J.; Kruth, J.P. Fatigue behaviour of NiTi shape memory alloy scaffolds produced by SLM, a unit cell design comparison. *J. Mech. Behav. Biomed. Mater.* **2017**, *70*, 53–59. [[CrossRef](#)]
23. LePage, W.S.; Shaw, J.A.; Daly, S.H. Effects of texture on the functional and structural fatigue of a NiTi shape memory alloy. *Int. J. Solids Struct.* **2021**, *221*, 150–164. [[CrossRef](#)]
24. Bagheri, A.; Mahtabi, M.J.; Shamsaei, N. Fatigue behavior and cyclic deformation of additive manufactured NiTi. *J. Am. Acad. Dermatol.* **2018**, *252*, 440–453. [[CrossRef](#)]
25. Bayati, P.; Jahadakbar, A.; Barati, M.; Nematollahi, M.; Saint-Sulpice, L.; Haghshenas, M.; Chirani, S.A.; Mahtabi, M.J.; Elahinia, M. Toward low and high cycle fatigue behavior of SLM-fabricated NiTi: Considering the effect of build orientation and employing a self-heating approach. *Int. J. Mech. Sci.* **2020**, *185*, 105878. [[CrossRef](#)]
26. Hartl, D.J.; Mabe, J.H.; Benafan, O.; Coda, A.; Conduit, B.; Padan, R.; Doren, B.V. Standardization of shape memory alloy test methods toward certification of aerospace applications. *Smart Mater. Struct.* **2015**, *24*, 082001. [[CrossRef](#)]
27. Doudard, C.; Calloch, S.; Cugy, P.; Galtier, A.; Hild, F. A probabilistic two-scale model for high-cycle fatigue life predictions. *Fatigue Fract. Eng. Mater. Struct.* **2005**, *28*, 279–288. [[CrossRef](#)]
28. Munier, R.; Doudard, C.; Calloch, S.; Weber, B. Determination of high cycle fatigue properties of a wide range of steel sheet grades from self-heating measurements. *Int. J. Fatigue* **2014**, *63*, 46–61. [[CrossRef](#)]
29. Amini, B.; Demmouche, Y.; Barati, M.; Helbert, G.; Chirani, S.A.; Calloch, S. Self-heating of metastable 304L austenitic stainless steel under cyclic loading: Influence of initial martensite volume fraction, testing temperature and pre-strain. *Mech. Mater.* **2020**, *151*, 103596. [[CrossRef](#)]
30. Bercelli, L. Étude des Propriétés en Fatigue Polycyclique des matériaux et des Structures Obtenus par le Procédé de Fabrication Additive Arc-Fil. Ph.D. Thesis., ENSTA Bretagne-École Nationale Supérieure de Techniques Avancées Bretagne: Brest, France, 2021.
31. Munier, R.; Doudard, C.; Calloch, S.; Weber, B.; Facchinetti, M. Contribution of Kinematical and Thermal Full-field Measurements for Mechanical Properties Identification: Application to High Cycle Fatigue of Steels. *Exp. Mech.* **2011**, *52*, 743–756. [[CrossRef](#)]

32. Ezanno, A.; Doudard, C.; Calloch, S.; Heuzé, J.L. A new approach to characterizing and modeling the high cycle fatigue properties of cast materials based on self-heating measurements under cyclic loadings. *Int. J. Fatigue* **2013**, *47*, 232–243. [[CrossRef](#)]
33. Louge, J.; Munier, R.; Doudard, C.; Calloch, S.; Weber, B. Two new in-plane torsion tests for the investigation of self-heating under pure shear cyclic loading. *Int. J. Fatigue* **2021**, *149*, 106256. [[CrossRef](#)]
34. Doudard, C.; Calloch, S. Influence of hardening type on self-heating of metallic materials under cyclic loadings at low amplitude. *Eur. J. Mech. A/Solids* **2009**, *28*, 233–240. [[CrossRef](#)]
35. Jegou, L.; Marco, Y.; Le Saux, V.; Calloch, S. Fast prediction of the Wöhler curve from heat build-up measurements on Short Fiber Reinforced Plastic. *Int. J. Fatigue* **2013**, *47*, 259–267. [[CrossRef](#)]
36. Peyrac, C.; Jollivet, T.; Leray, N.; Lefebvre, F.; Westphal, O.; Gornet, L. Self-heating Method for Fatigue Limit Determination on Thermoplastic Composites. *Procedia Eng.* **2015**, *133*, 129–135. [[CrossRef](#)]
37. Le Saux, V.; Marco, Y.; Calloch, S.; Doudard, C.; Charrier, P. Fast evaluation of the fatigue lifetime of rubber-like materials based on a heat build-up protocol and micro-tomography measurements. *Int. J. Fatigue* **2010**, *32*, 1582–1590. [[CrossRef](#)]
38. Mostofizadeh, P.; Kадkhodaei, M.; Arbab Chirani, S.; Saint-Sulpice, L.; Rokbani, M.; Bouraoui, T.; Calloch, S. Fatigue analysis of shape memory alloys by self-heating method. *Int. J. Mech. Sci.* **2019**, *156*, 329–341. [[CrossRef](#)]
39. Saint-Sulpice, L.; Legrand, V.; Arbab-Chirani, S.; Calloch, S.; Doudard, C. Fatigue life study of superelastic NiTi Shape Memory Alloys using self-heating under cyclic loading method. *Int. J. Fatigue* **2022**, *165*, 107208. [[CrossRef](#)]
40. Shayesteh Moghaddam, N.; Saedi, S.; Amerinatanzi, A.; Hinojos, A.; Ramazani, A.; Kundin, J.; Mills, M.J.; Karaca, H.; Elahinia, M. Achieving superelasticity in additively manufactured NiTi in compression without post-process heat treatment. *Sci. Rep.* **2019**, *9*, 41. [[CrossRef](#)]
41. Saedi, S.; Shayesteh Moghaddam, N.; Amerinatanzi, A.; Elahinia, M.; Karaca, H.E. On the effects of selective laser melting process parameters on microstructure and thermomechanical response of Ni-rich NiTi. *Acta Mater.* **2018**, *144*, 552–560. [[CrossRef](#)]
42. Sitzman, S.; Nolze, G.; Nowell, M. EBSD Pattern Quality and its Use in Evaluating Sample Surface Condition. *Microsc. Microanal.* **2010**, *16*, 698–699. [[CrossRef](#)]
43. Bernard, S.; Krishna Balla, V.; Bose, S.; Bandyopadhyay, A. Compression fatigue behavior of laser processed porous NiTi alloy. *J. Mech. Behav. Biomed. Mater.* **2012**, *13*, 62–68. [[CrossRef](#)]
44. Charkaluk, E.; Constantinescu, A. Dissipative aspects in high cycle fatigue. *Mech. Mater.* **2009**, *41*, 483–494. [[CrossRef](#)]
45. Nematollahi, M.; Saghalian, S.E.; Safaei, K.; Bayati, P.; Bassani, P.; Biffi, C.; Tuissi, A.; Karaca, H.; Elahinia, M. Building orientation-structure-property in laser powder bed fusion of NiTi shape memory alloy. *J. Alloy. Compd.* **2021**, *873*, 159791. [[CrossRef](#)]
46. Masuo, H.; Tanaka, Y.; Morokoshi, S.; Yagura, H.; Uchida, T.; Yamamoto, Y.; Murakami, Y. Influence of defects, surface roughness and HIP on the fatigue strength of Ti-6Al-4V manufactured by additive manufacturing. *Int. J. Fatigue* **2018**, *117*, 163–179. [[CrossRef](#)]
47. Snopiński, P. Effects of KoBo-Processing and Subsequent Annealing Treatment on Grain Boundary Network and Texture Development in Laser Powder Bed Fusion (LPBF) AlSi10Mg Alloy. *Symmetry* **2024**, *16*, 122. [[CrossRef](#)]
48. Carlucci, G.; Patriarca, L.; Demir, A.G.; Lemke, J.N.; Coda, A.; Previtali, B.; Casati, R. Building Orientation and Heat Treatments Effect on the Pseudoelastic Properties of NiTi Produced by LPBF. *Shape Mem. Superelasticity* **2022**, *8*, 235–247. [[CrossRef](#)]
49. Munier, R.; Doudard, C.; Calloch, S.; Weber, B. Identification of the micro-plasticity mechanisms at the origin of self-heating under cyclic loading with low stress amplitude. *Int. J. Fatigue* **2017**, *103*, 122–135. [[CrossRef](#)]
50. Kudoh, Y.; Tokonami, M.; Miyazaki, S.; Otsuka, K. Crystal structure of the martensite in Ti-49.2 at.%Ni alloy analyzed by the single crystal X-ray diffraction method. *Acta Met.* **1985**, *33*, 2049–2056. [[CrossRef](#)]
51. Otsuka, K.; Ren, X. Physical metallurgy of Ti-Ni-based shape memory alloys. *Prog. Mater. Sci.* **2005**, *50*, 511–678. [[CrossRef](#)]
52. Teramoto, T.; Tahara, M.; Hosoda, H.; Inamura, T. Compatibility at Junction Planes between Habit Plane Variants with Internal Twin in Ti-Ni-Pd Shape Memory Alloy. *Mater. Trans.* **2016**, *57*, 233–240. [[CrossRef](#)]
53. Liu, Y. The superelastic anisotropy in a NiTi shape memory alloy thin sheet. *Acta Mater.* **2015**, *95*, 411–427. [[CrossRef](#)]
54. Mao, S.C.; Luo, J.F.; Zhang, Z.; Wu, M.H.; Liu, Y.; Han, X.D. EBSD studies of the stress-induced B2–B19' martensitic transformation in NiTi tubes under uniaxial tension and compression. *Acta Mater.* **2010**, *58*, 3357–3366. [[CrossRef](#)]
55. Pant, P.; Salvemini, F.; Proper, S.; Luzin, V.; Simonsson, K.; Sjöström, S.; Hosseini, S.; Peng, R.L.; Moverare, J. A study of the influence of novel scan strategies on residual stress and microstructure of L-shaped LPBF IN718 samples. *Mater. Des.* **2022**, *214*, 110386. [[CrossRef](#)]
56. Andreau, O.; Koutiri, I.; Peyre, P.; Penot, J.D.; Saintier, N.; Pessard, E.; De Terris, T.; Dupuy, C.; Baudin, T. Texture control of 316L parts by modulation of the melt pool morphology in selective laser melting. *J. Am. Acad. Dermatol.* **2018**, *264*, 21–31. [[CrossRef](#)]
57. Zhou, X.; Li, K.; Zhang, D.; Liu, X.; Ma, J.; Liu, W.; Shen, Z. Textures formed in a CoCrMo alloy by selective laser melting. *J. Alloy. Compd.* **2015**, *631*, 153–164. [[CrossRef](#)]
58. Polák, J. Role of Persistent Slip Bands and Persistent Slip Markings in Fatigue Crack Initiation in Polycrystals. *Crystals* **2023**, *13*, 220. [[CrossRef](#)]
59. Suresh, S. *Fatigue of Materials*, 2nd ed.; Cambridge University Press: Cambridge, UK, 1998. [[CrossRef](#)]
60. Differt, K.; Esmann, U.; Mughrabi, H. A model of extrusions and intrusions in fatigued metals II. Surface roughening by random irreversible slip. *Philos. Mag. A* **1986**, *54*, 237–258. [[CrossRef](#)]

61. Polatidis, E.; Šmíd, M.; Kuběna, I.; Hsu, W.N.; Laplanche, G.; Van Swygenhoven, H. Deformation mechanisms in a superelastic NiTi alloy: An in-situ high resolution digital image correlation study. *Mater. Des.* **2020**, *191*, 108622. [[CrossRef](#)]
62. Li, W.; Lee, S.; Zhang, T.; Jin, Y.; Pagan, D.; Casalena, L.; Mills, M.; Bucsek, A. 3D in-situ characterization of dislocation density in nickel-titanium shape memory alloys using high-energy diffraction microscopy. *Acta Mater.* **2024**, *266*, 119659. [[CrossRef](#)]
63. Pelton, A.R. Nitinol Fatigue: A Review of Microstructures and Mechanisms. *J. Mater. Eng. Perform.* **2011**, *20*, 613–617. [[CrossRef](#)]
64. Zheng, L.; He, Y.; Moumni, Z. Effects of Lüders-like bands on NiTi fatigue behaviors. *Int. J. Solids Struct.* **2016**, *83*, 28–44. [[CrossRef](#)]
65. Zhang, Y.; You, Y.; Moumni, Z.; Anlas, G.; Zhu, J.; Zhang, W. Experimental and theoretical investigation of the frequency effect on low cycle fatigue of shape memory alloys. *Int. J. Plast.* **2017**, *90*, 1–30. [[CrossRef](#)]
66. Kockar, B.; Karaman, I.; Kim, J.I.; Chumlyakov, Y.I.; Sharp, J.; Yu, C.J.M. Thermomechanical cyclic response of an ultrafine-grained NiTi shape memory alloy. *Acta Mater.* **2008**, *56*, 3630–3646. [[CrossRef](#)]
67. Pelton, A.R.; Huang, G.H.; Moine, P.; Sinclair, R. Effects of thermal cycling on microstructure and properties in Nitinol. *Mater. Sci. Eng. A* **2012**, *532*, 130–138. [[CrossRef](#)]
68. Sangid, M.D.; Maier, H.J.; Sehitoglu, H. The role of grain boundaries on fatigue crack initiation—An energy approach. *Int. J. Plast.* **2011**, *27*, 801–821. [[CrossRef](#)]
69. Alarcon, E.; Heller, L.; Chirani, S.A.; Šittner, P.; Kopeček, J.; Saint-Sulpice, L.; Calloch, S. Fatigue performance of superelastic NiTi near stress-induced martensitic transformation. *Int. J. Fatigue* **2017**, *95*, 76–89. [[CrossRef](#)]

Disclaimer/Publisher’s Note: The statements, opinions and data contained in all publications are solely those of the individual author(s) and contributor(s) and not of MDPI and/or the editor(s). MDPI and/or the editor(s) disclaim responsibility for any injury to people or property resulting from any ideas, methods, instructions or products referred to in the content.